



VYSOKÉ UČENÍ TECHNICKÉ V BRNĚ
BRNO UNIVERSITY OF TECHNOLOGY



FAKULTA STROJNÍHO INŽENÝRSTVÍ
ÚSTAV MATEMATIKY
FACULTY OF MECHANICAL ENGINEERING
INSTITUTE OF MATHEMATICS

NEW APPROACHES IN AIRBORNE THERMAL IMAGE PROCESSING FOR LANDSCAPE ASSESSMENT

NOVÉ PŘÍSTUPY ZPRACOVÁNÍ LETECKÝCH OBRAZOVÝCH TERMÁLNÍCH DAT K
HODNOCENÍ KRAJINY

DISERTAČNÍ PRÁCE
DOCTORAL THESIS

AUTOR PRÁCE
AUTHOR

Ing. MAREK PIVOVARNÍK

VEDOUCÍ PRÁCE
SUPERVISOR

doc. Mgr. Ing. FRANTIŠEK ZEMEK, Ph.D.

Abstrakt

TO DO...

Summary

TO DO...

Klíčová slova

diaľkový prieskum Zeme, letecké termálne hyperspektrálne dáta, separácia teploty a emissivity

Keywords

remote sensing, airborne thermal hyperspectral data, temperature-emissivity separation

Contents

1	Theoretical Background on Thermal Radiation	9
2	Airborne Thermal Hyperspectral Data Properties	13
2.1	Instrument Technical Specifications	13
2.2	Image pre-processing	14
3	Temperature and Emissivity Separation	21
3.1	Available approaches	21
3.2	TES Algorithm Improvement	24
3.3	Algorithm Performance	25
3.4	Simulated Data	26
3.5	Comparison with ASTER standard products	27
3.6	Application to TASI Data	30
4	Ground Measurements	31
4.1	Libraries	31
4.2	Technical Specifications	31
4.3	Instrument Calibration	31
4.4	Temperature and Emissivity Separation	31
4.5	Applications	31
5	Application to UHI Detection	33
6	Conclusion	35
	References	37
	References	37

CONTENTS

Theoretical Background on Thermal Radiation

This chapter describes fundamental principles and concepts of EM radiation called *thermal radiation*. Every object with temperature above 0 K emits thermal radiation. The amount of thermal radiation as a function of wavelength depends on object's temperature and its surface as is described in following text.

Black body

The concept of black body is very well described in the work of Howell [12], where black body is defined as perfect absorber for all incident radiation. Apart of perfect absorber, the black body is perfect emitter as well. Thus black body absorbs and reemits all energy incident upon it. Black body does not exist in nature but its concept is used for determination of real object's surface property called emissivity, which will be defined in following text.

Planck's law

Concerning black body at thermal equilibrium, the amount and spectral distribution of emitted energy is described by Planck's law [20]:

$$B(T, \lambda) = \frac{2hc^2}{\lambda^5} \frac{1}{e^{\frac{hc}{\lambda kT}} - 1},$$

where $B(T, \lambda)$ is spectral radiance ($\text{W m}^{-2} \mu\text{m}^{-1} \text{sr}^{-1}$) of black body at temperature T (K) and wavelength λ (μm); k is Boltzmann constant ($1.3806488 \cdot 10^{-23} \text{ J K}^{-1}$), h is Planck constant ($6.62606957 \cdot 10^{-34} \text{ Js}$) and c is speed of light ($299792458 \text{ m s}^{-1}$). Example of the black body radiation at three different temperatures, as described by Planck's law, is depicted in figure 3.2a.

Emissivity

The emissivity is defined as ratio of radiance of real surface to that of black body at the same temperature:

$$\varepsilon(T, \lambda) = \frac{L(T, \lambda)}{B(T, \lambda)},$$

where $\varepsilon(T, \lambda)$ is spectral emissivity and $L(T, \lambda)$ is real surface spectral radiance. The emissivity can be understood as real surface emission effectiveness in comparison with radiation emitted by a black body of the same temperature in the same wavelength. Let us note that emissivity depends on the viewing angle apart temperature and wavelength, as is defined in Hollow [12]. In remote sensing an observed objects are of the temperature within 270 – 330 K and the observation angle is close to nadir (usually maximum off-nadir angle is less than 30°), which causes negligible changes in spectral emissivity of most of the natural surfaces. Thus, it can be further assumed that emissivity depends just on wavelength.

Quartz was chosen to demonstrate the principles of radiation of real object's surfaces. Its spectral emissivity was taken from ASTER spectral library [1] and it is shown in the figure 3.2b. Quartz heated to the temperature T has spectral radiance $L(T, \lambda) = \varepsilon(\lambda)B(T, \lambda)$ as is illustrated in figure 3.2c.

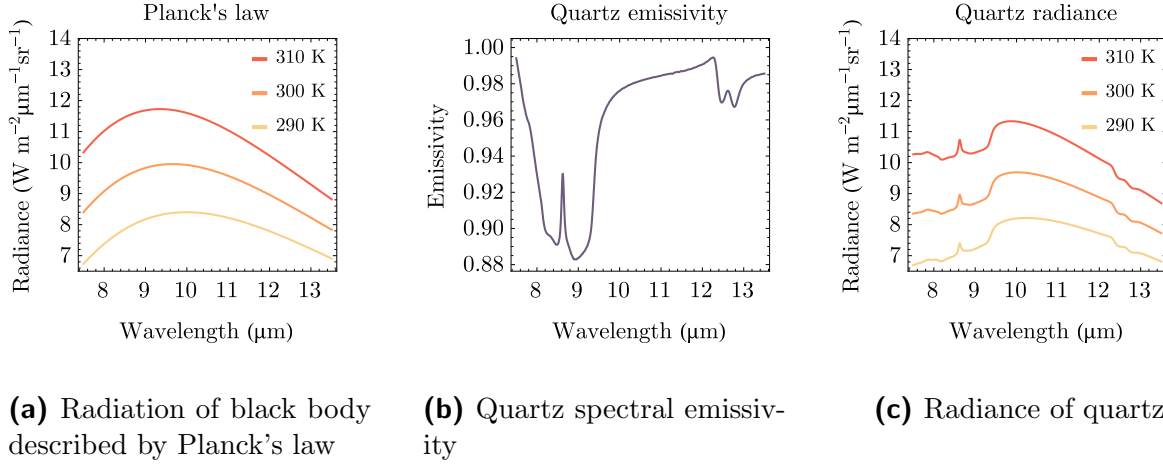


Figure 1.1: Principles of radiation of real surfaces.

Wien's displacement law

The peak of black body radiation at wavelength λ_{max} is described by Wien's displacement law [12]:

$$\lambda_{max} = \frac{b}{T},$$

where b is Wien's displacement constant (2.8977721 m K). As was mentioned before, the temperature of the most of the natural and artificial surfaces observed by airborne remote sensing ranges in 270 – 330 K. According to the Wien's displacement law, the peak of emitted radiation varies roughly from 8.8 μm to 10.7 μm . This range is in coincidence with the atmospheric window situated between 8 μm to 13 μm . The atmospheric transmittance in this atmospheric window is very high and thus it is relevant for acquisition of remotely sensed thermal data.

Kirchhoff's law of thermal radiation

Emitting and absorbing properties of an object at local thermodynamic equilibrium surrounded by isothermal environment are tied up by Kirchhoff's law of thermal radiation

[14]. It states that object's surface absorptivity $\alpha(\lambda)$ at a given wavelength equals to object surface emissivity $\varepsilon(\lambda)$ at the same wavelength:

$$\alpha(\lambda) = \varepsilon(\lambda).$$

Energy conservation implies that energy incident to the object surface can be reflected, transmitted or absorbed. Considering the fractions of incident energy the following equation holds:

$$1 = \rho(\lambda) + \tau(\lambda) + \alpha(\lambda),$$

where $\rho(\lambda)$ is objects surface spectral reflectivity, $\tau(\lambda)$ is object surface spectral transmissivity and $\alpha(\lambda)$ is object surface spectral absorptivity. Applying Kirchhoff's law to opaque material ($\tau(\lambda) = 0$) results in following equation:

$$1 = \rho(\lambda) + \varepsilon(\lambda) \quad \Rightarrow \quad \rho(\lambda) = 1 - \varepsilon(\lambda).$$

All mentioned principles in this section will be further used in explanation of properties of airborne thermal hyperspectral data and its processing.

Airborne Thermal Hyperspectral Data Properties

This chapter provides insights into technical parameters of Thermal Airborne Spectrographic Imager (TASI) and processing chain of images acquired by this sensor. Knowledge of the instrument parameters and processing chain gives important overview of the data properties and their components. The result of the processing chain described in this chapter is georeferenced image containing land-leaving radiance. Such an image forms input for further processing. Let us note that this chapter omits naming physical quantities dependent on wavelength as “spectral” for the sake of clarity. However, all quantities remain wavelength dependent.

2.1. Instrument Technical Specifications

The TASI sensor is developed by Itres Ltd. (Calgary, Canada) and is one of the very few commercially available pushbroom hyperspectral TIR sensors equipped with mercury cadmium telluride array. Each of its 600 across-track imaging pixels contains 32 bands all of which are in the TIR region. Bands are situated in the 8 to 11.5 μm region and have a FWHM $\approx 0.11 \mu\text{m}$ with $\text{NE}\Delta T \approx 0.1$. The response functions of the TASI sensor are described by the Gaussian functions as depicted in Figure 2.6a.

The shape of response functions implies that any quantity observed by TASI sensor is of finite spectral-bandwidth. Quantities needs to be transformed to band-effective quantities in order to relate them with certain wavelength. The band-effective quantities are obtained by using weighted average:

$$X_i = \frac{\int_{\lambda_1}^{\lambda_2} r_i(\lambda) X(\lambda) d\lambda}{\int_{\lambda_1}^{\lambda_2} r_i(\lambda) d\lambda}, \quad (2.1)$$

where $r_i(\lambda)$ is response function of band i , λ_1 and λ_2 are lower and upper boundaries of band i and X can be substituted by any quantity. In Figure 2.6b is illustrated radiance of quartz (solid line) and band-effective values of radiance measured by the TASI sensor (green dots). Sensor of this type is available at Global Change Research Institute CAS (Brno, Czech Republic) and it is a part of Flying Laboratory Of Imaging Systems (FLIS) [11].

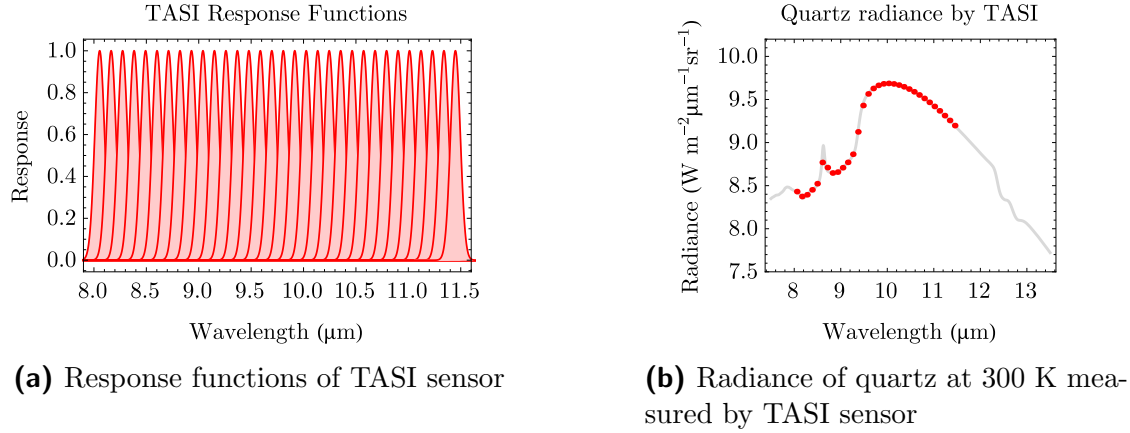


Figure 2.1: TASI response functions.

2.2. Image pre-processing

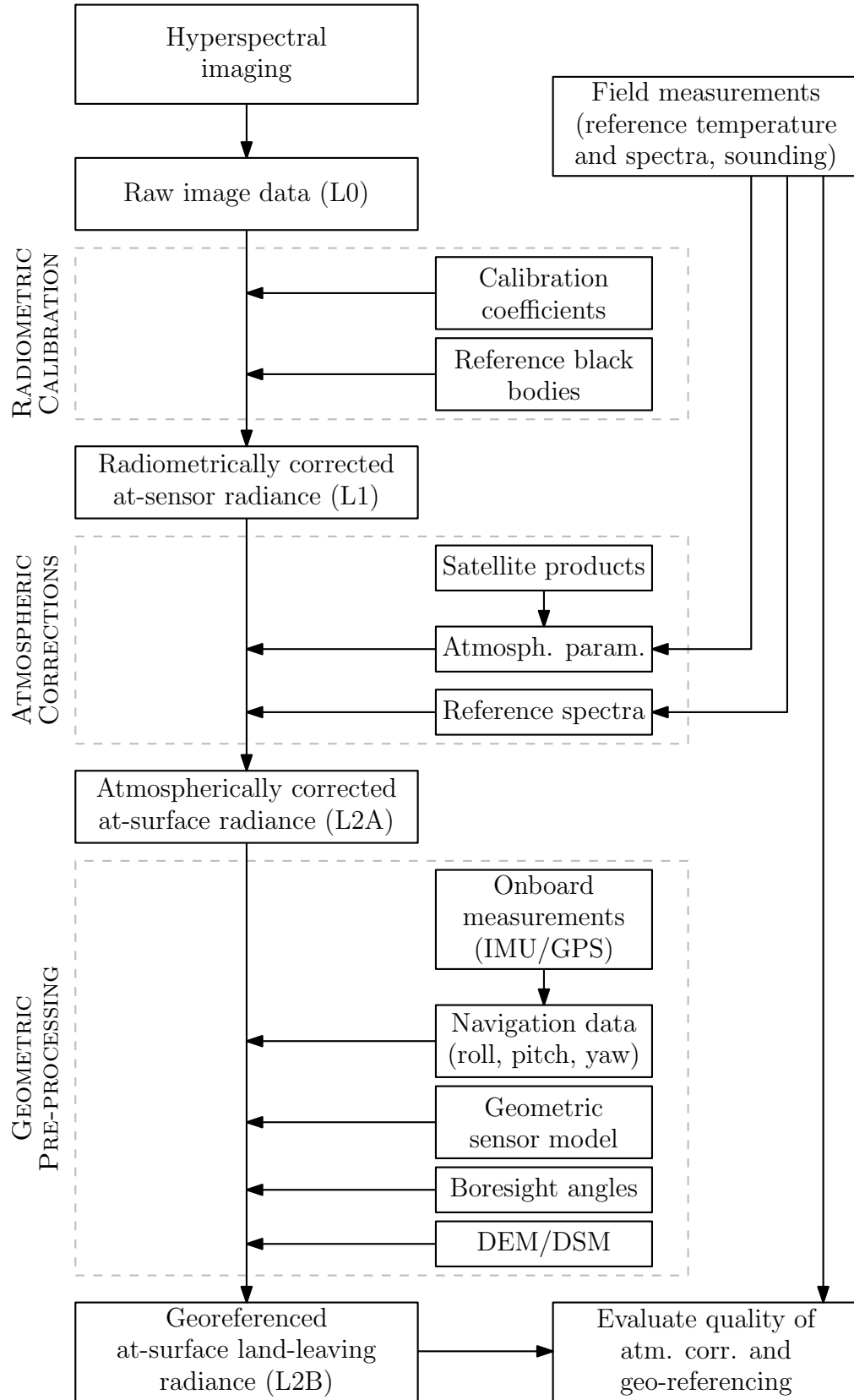
The main objective of image pre-processing is transformation of acquired raw image into the georeferenced radiance at-surface level. It is accomplished by three major steps: radiometric calibration, atmospheric corrections and geometric pre-processing. Radiometric calibration converts digital numbers (DN) into values of radiance at-sensor level. Atmospheric corrections compensates the influence of intervening atmosphere and produces land-leaving radiance. Finally, the geometric pre-processing compensates for image distortions caused by airplane movement and register image into coordinate system.

Supportive field measurements of thermal radiance, temperature, emissivity and atmosphere parameters offers valuable data for calibration and validation purposes. Especially in cases of airborne images for scientific purposes the high quality is strongly demanding. Thus it is necessary to perform supportive measurements in order to achieve precise results and determine the data quality.

It is important to emphasize, that currently does not exist any definitive standard pre-processing chain. It is caused mainly by huge number of sensors with various technical parameters and their different applications. Sensors usually have tailored pre-processing chains, which is the case of TASI sensor as well. Certain parts of processing chain are maintained by commercial tools. However, there are still parts of processing chain, which needs to be done by in-house tools. In Figure 2.2 is illustrated processing chain used in Global Change Research Institute CAS (Brno, Czech Republic) to pre-process image acquired by TASI sensor. Individual parts of the diagram will be discussed in the following text.

2.2.1. Radiometric Calibration

Thermal radiation incident upon the sensor array originates from many additive components (e.g. observed scene, instrument enclosure, intervening atmosphere and others). Incident thermal radiation produces electrical signal, which is proportional to radiant intensity. Electrical signal is then amplified and converted into voltage and subsequently into DN values. Radiometric calibration consists of separating signal from viewed scene

**Figure 2.2:** Processing chain.

and converting it into physical units of radiance. Atmosphere influence is not accounted in this process and thus after radiometric calibration one gets radiance at-sensor level.

The relationship between DN and at-sensor radiance L_m is following:

$$DN = a + bL_m,$$

where a and b are calibration coefficients. The calibration coefficient a , also known as offset, represents radiation originating from instrument enclosure, sensor dark current and electronic offset. The calibration coefficient b , also called gain, determines sensor radiant sensitivity. Calibration coefficients are determined by imaging a set of reference black bodies of known temperature and emissivity. In this context, the term black body is ment to be a surface with emissivity very close to unity. These coefficients are usually determined applying one of two methods: 1) imaging two black bodies at different temperature directly before imaging, or 2) combining black body measurements from laboratory and black body image acquired before imaging.

In the first case are usually used two black bodies of different temperatures. Temperatures of these black bodies enclose temperatures expected to occur in the scene. Let us consider the radiance of cold black body $L(T_C)$ and the radiance of hot blackbody $L(T_H)$. The calibration coefficients can be obtained from:

$$\begin{aligned} a &= \frac{DN_H L(T_C) - DN_C L(T_H)}{L(T_C) - L(T_H)} \\ b &= \frac{DN_C - DN_H}{L(T_C) - L(T_H)}, \end{aligned}$$

where DN_C and DN_H are digital numbers measured by sensor viewing cold black body and hot black body respectively. This procedure is commonly used in case of other instruments for measuring thermal radiation, such as μ FTIR ??.

The determination of calibration coefficients in the second case assumes that gain calibration coefficient b does not change under different conditions. Thus, it is sufficient to perform series of black body measurements at different temperatures in order to determine gain calibration coefficient b . These measurements can be performed in the laboratory once per season. However, offset calibration coefficient a does not remain stable and changes under different conditions. Hence, it is necessary to image a black body at known temperature directly before acquisition to account for variability of this coefficient.

Again, it is important to emphasize that all quantities and both calibration coefficients are wavelength dependent. Spectral calibrations are part of the radiometric calibrations. In the laboratory are determined band centers of every pixel using laser at different wavelengths. Determined positions does not change over time significantly. However, the spectral shift occurs under different conditions and thus it needs to be determined for every scene. Spectral shift estimation is usually based on the spectral features of the atmosphere or certain materials.

In case of TASI sensor are used commercial softwares delivered by Itres company (Calgary, Canada). SparCal software [73] is used to determine all parameters necessary for radiometric calibrations from laboratory measurements. RCX software [74] is used for additional estimation of calibration parameters and for processing raw image. Both softwares are tailored for the TASI sensor. The resulting image is made of radiance at-sensor level L_m .

2.2.2. Atmospheric Corrections

Radiometric calibrations deliver image containing radiation from the surface, attenuated by atmosphere, plus radiation from the intervening atmosphere. Thus the measured radiance at-sensor level (L_m) consists mainly of radiance emitted from the land surface, downwelling atmospheric radiance reflected by the surface (L_{atm}^\downarrow) and the atmospheric upwelling radiance (L_{atm}^\uparrow). The sum of all these components is expressed by a radiative transfer equation (RTE) as follows:

$$L_m = \tau \varepsilon B(T_s) + \tau(1 - \varepsilon)L_{atm}^\downarrow + L_{atm}^\uparrow, \quad (2.2)$$

where $B(T_s)$ is radiance of the surface at temperature T_s according to the Planck's law, ε is the surface's emissivity and τ is atmospheric transmittance. It is important to emphasize that all elements in the equation are wavelength dependent but notation for this is omitted for the sake of clarity. Since sensors are of finite bandwidth, quantities in (2.2) are replaced by band-effective equivalents according to the equation (2.1). Moreover, RTE can be used under the assumption of cloud-free atmosphere under local thermodynamic equilibrium. The meaning of the RTE is illustrated in the Figure 2.3, where ρ is reflectivity. Kirchhoff's law of thermal radiation implies that reflectivity ρ can be rewritten as $(1 - \varepsilon)$ for opaque materials.

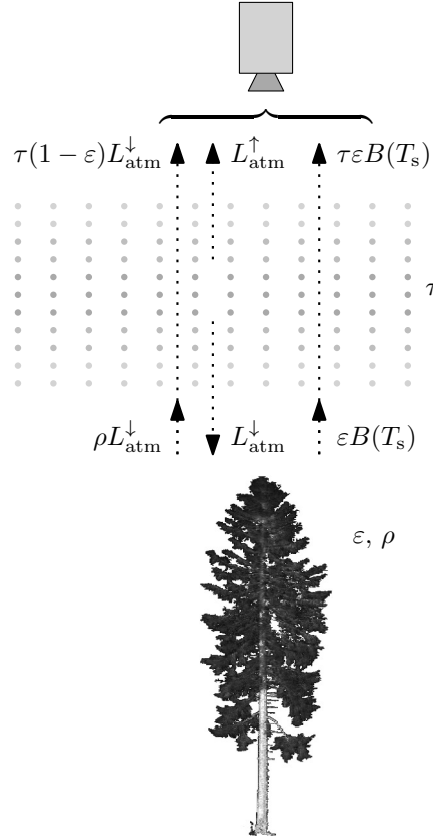


Figure 2.3: The radiance incident to the sensor in the thermal region originates mainly from three sources: 1) radiance $\tau \varepsilon B(T_s)$ emitted by object; 2) reflected downwelling atmospheric radiance $\tau(1 - \varepsilon)L_{atm}^\downarrow$; 3) upwelling atmospheric radiance L_{atm}^\uparrow emitted by atmosphere itself.

The goal of the atmospheric corrections is to determine atmospheric transmittance, downwelling and upwelling atmospheric radiance and compensate for them. The quantifi-

cation of these quantities are usually based on radiative transfer models of the atmosphere. For this purpose is usually used MODerate resolution atmospheric TRANsmission (MODTRAN) model [3]. MODTRAN simulates atmospheric parameters such as atmospheric transmittance, downwelling and upwelling atmospheric radiance based on input parameters such as vertical profiles of water vapour content and temperature, CO₂ concentration, the choice of model atmosphere (if measured profiles are not available) and many others. In general, input parameters can be obtained in two ways: 1) by in-situ measurements; 2) by satellite-based products.

The most common in-situ measurement is radio sounding. Radiosonde is launched during the overflight and it is used to measure vertical temperature and water vapour profile of the atmosphere. Other in-situ instruments can be used as well, for example sun-photometer for obtaining water vapor content or different radiometers for measuring sky or surface radiance. Other source of water vapour and temperature profile is satellite-based products acquired close to the time of aircraft overflight. The most common is MOD07_L2 product [4] generated by Moderate Resolution Imaging Spectroradiometer (MODIS) instrument [17]. Illustration of the transmittance, downwelling and upwelling atmospheric radiance generated by MODTRAN using MOD07_L2 products as input are depicted in Figure 2.4.

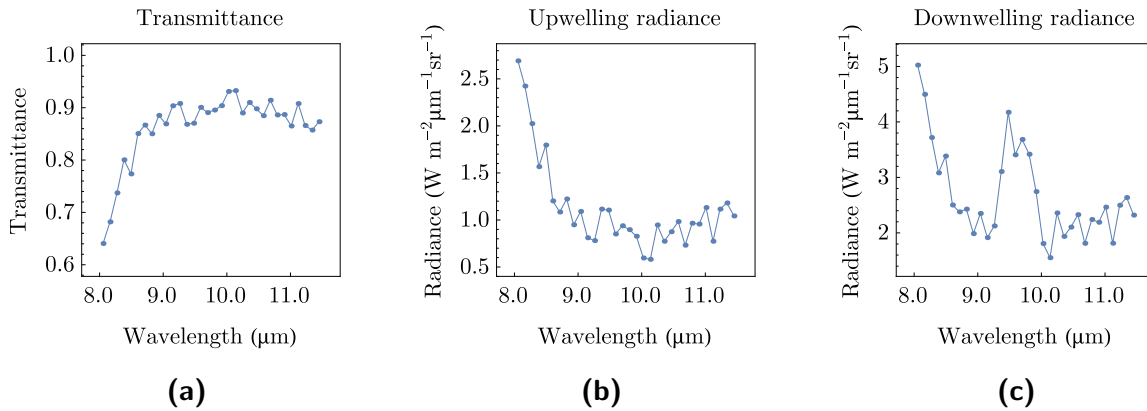


Figure 2.4: Example of atmospheric parameters used for atmospheric correction of TASI image acquired at altitude of 2000 m during summer season.

In case of thermal hyperspectral images, various algorithms for estimating atmospheric effects based just on the image itself were developed. Usually it is applied to one of the following: In-Scene Atmospheric Corrections (ISAC) introduced by Young et al. [30] and Autonomous Atmospheric Compensation (AAC) introduced by Gu et al. [10]. The advantage of using one of these algorithms is that no supporting data are necessary. The drawback of these methods remains in estimation of just atmospheric transmittance and upwelling atmospheric radiance.

Once all the atmospheric parameters are determined, it remains to compensate for them. Compensating for atmospheric transmittance and upwelling atmospheric radiance lead to land-leaving radiance:

$$L_{LL} = \varepsilon B(T_s) + (1 - \varepsilon)L_{\text{atm}}^{\downarrow}. \quad (2.3)$$

The downwelling atmospheric radiance is not possible to separate without knowledge of emissivity. Hence, image after atmospheric corrections is made of land-leaving radiance

L_{LL} . Compensation for downwelling atmospheric radiance is part of the temperature and emissivity separation described in Chapter 3.

Atmospheric corrections for TASI sensor, as part of processing chain, are not performed by commercial products. However, there exists commercial tools that allows complex solution for atmospheric corrections. An example of such a tool is ATCOR [23] which is based on look-up tables generated by MODTRAN and takes into account terrain topography and sensor parameters. It offers basic temperature and emissivity separation algorithms as well. Apart of mentioned solution, atmospheric corrections rely on extracting data from in-situ measurements or satellite products, running radiative transfer models and applying derived atmospheric parameter on image. Alternatively, algorithms for atmospheric parameters estimation from image can be implemented. In both cases, atmospheric corrections involve creating in-house tools.

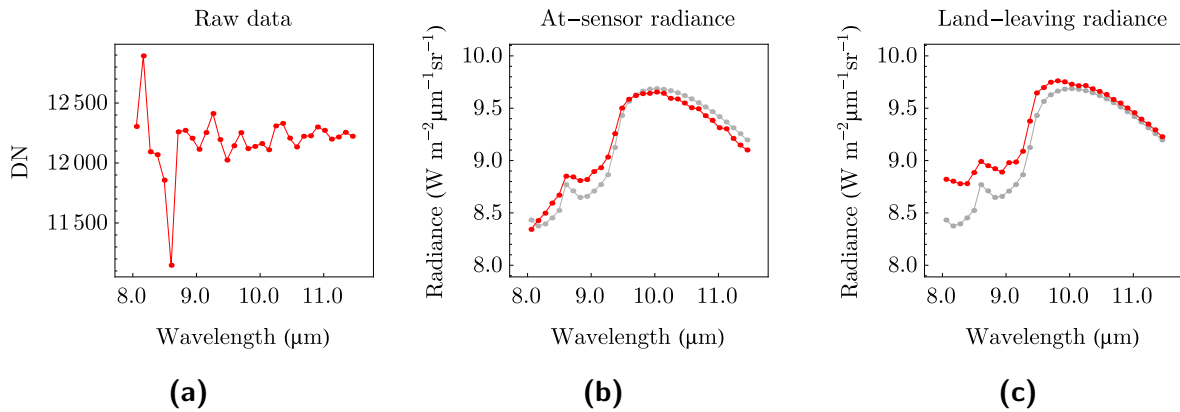


Figure 2.5: Simulation of airborne image of quartz at 300 K acquired by TASI sensor at altitude of 2000 m under summer mid-latitude atmosphere and illustration of radiometric calibration and atmospheric corrections. Case (a) shows raw data, case (b) shows data after radiometric calibration (in red) and case (c) shows data after corrections of atmospheric transmissivity and upwelling atmospheric radiance (in red). In cases (b) and (c) are shown pure quartz radiance in gray.

2.2.3. Geometric Pre-processing

Acquired image is distorted during its acquisition and geometric pre-processing is accounting for all factors causing these distortions. During geometric pre-processing are taken into account aircraft motion, terrain variations, geometric sensor model and boresight angles in order to register image into reference frame.

Ancillary data about aircraft position and movement, terrain structure, geometric sensor model and boresight angles are necessary. Aircrafts are nowadays equipped with IMU/GNSS systems for recording aircraft position (longitude, latitude and altitude) and orientation (roll, pitch and heading angles). Terrain structure is obtained from Digital Surface Model (DSM) or Digital Elevation Model (DEM). These data are derived from aerial laser scanning or from stereo images. Aerial laser scanning can be performed either simultaneously with image acquisition or separately. Other sources of DEM/DSM are national services or satellite products (e.g. ASTER product AST14DEM). Geometric sensor model is usually delivered by sensor manufacturer. Finally, boresight angles accounts for

different position of IMU/GNSS system and sensor optics. Boresight angles are derived from the set of Ground Control Points (GCPs) with known geographic coordinates, which are identified in the acquired image.

Geo-referencing consists of image orthogonalization and image resampling into regular grid of the reference frame with the desired coordinate system (e.g. Universal Transverse Mercator coordinate system). Image is resampled into desired spatial resolution applying nearest neighbour, bilinear or cubic interpolation. For the scientific purposes is commonly used nearest neighbour interpolation since it preserves spectral information and does not combine spectra from surrounding pixels.

Geometric pre-processing of the images acquired by TASI sensor are performed by GCSS software [75] delivered by Itres company (Calgary, Canada). Boresight angles are determined on the set of CGPs and images of Modřice in the case of campaigns held in the region of Czech Republic. Importance of image geometric pre-processing is illustrated in the Figure 2.6.



(a) Distorted image



(b) Georeferenced image

Figure 2.6: Illustration of land-leaving radiance image before and after geometric pre-processing.

Temperature and Emissivity Separation

Many applications of airborne thermal hyperspectral data are based on derivation of temperature and emissivity from the pre-processed image. These quantities are obtained from the system of RTEs. Let us remind that every spectral band follows RTE as shown in 2.2. Thus, in the case of TASI sensor one obtains system of 32 RTEs. Atmospheric transmittance τ , atmospheric upwelling radiance $L_{\text{atm}}^{\uparrow}$ and atmospheric downwelling radiance $L_{\text{atm}}^{\downarrow}$ are determined during atmospheric corrections as discussed in the Chapter 2. Note that even after the compensation of the atmosphere, the system of RTEs in case of TASI sensor contains 32 unknown emissivities and also unknown temperature, which is the same in all spectral bands. It results in the underdetermined system of equations. The estimation of temperature and emissivity from such a system of equations is usually addressed as temperature-emissivity separation. This chapter describes several approaches for separating temperature and emissivity. It firstly introduces few commonly used ones and then focuses on the most popular approach called *Temperature and emissivity separation algorithm*. Finally it discusses its possible improvement together with its validation.

3.1. Available approaches

Algorithms used for processing airborne thermal hyperspectral data are mostly focused on atmospheric correction and on estimation of temperature and emissivity. Procedures and algorithms for atmospheric correction will be mentioned just briefly. The attention will be focused on algorithms used for estimation of temperature and emissivity since this topic is further investigated as reported in section four.

Methods used to overcome the problem of underdetermined system of RTEs are usually based on adding empirical or semiempirical constraints. Review written by Li et al. [15] sums up currently used methods for spaceborne sensors. Just a few of the methods can be applied for processing of data from airborne sensors. The main reason is that satellites acquires images periodically and algorithms takes advantage of it. This requirement is difficult to fulfill with thermal airborne sensors. In following are mentioned four algorithms, which are commonly used in processing of airborne thermal hyperspectral data.

Gray body emissivity method

Barducci and Pippi [2] proposed algorithm, which is based on assumption of flat spectral emissivity beyond 10 μm . To solve the system of RTEs it is enough to find at least two

spectral bands with the same emissivity. This can be achieved in case of airborne thermal hyperspectral data. Drawback of this method is its sensitivity to instrument noise.

Linear emissivity constraint temperature emissivity separation method

As Wang et al. [29] describe, this method is based on idea of substituting spectral emissivity with piecewise linear function. The emissivity spectrum is divided into segments, in which spectral emissivities are assumed to be linearly dependent on wavelength. Thus, it is necessary for every segment to estimate gain and offset. It implies that the number of spectral bands has to be equal or greater than number of unknowns resulting from segmentation to piecewise linear functions.

Spectral smoothing

Spectral smoothing algorithm, also known as ARTEMIS (Automatic Retrieval of Temperature and EMISSivity using Spectral Smoothness), was reported by Borel at [5] and [6]. Algorithm is based on the assumption that spectra of solids are much more smoother than spectra of gases. Thus by smoothing spectra one removes spectral features introduced by atmosphere and obtains spectral emissivity. Moreover, current implementation described in [6] includes modified ISAC algorithm called ARTISAC, which estimates atmospheric transmissivity for further choice correct atmospheric model. Atmospheric models contains so called TUD (atmospheric Transmissivity, Upwelling and Downwelling atmospheric radiance) and are stored in look-up tables (LUT). Then temperature is varied until the spectral emissivity is the smoothest possible, where the smoothness criterion is standard deviation of measured radiance minus simulated radiance. Spectral smoothness method can be described briefly by following steps:

1. estimation atmospheric transmissivity using ARTISAC algorithm
2. determination few closest atmosphere models from TUD-LUT according to the estimated atmospheric transmissivity
3. use these atmosphere models as input to spectral smoothness algorithm for a few pixels chosen from the image and the atmosphere model which results in smoothest emissivity in the most of the cases is chosen as the correct one
4. use chosen atmosphere model for the whole image and estimate temperature and emissivity using spectral smoothness

Temperature and emissivity separation algorithm

Temperature and emissivity separation algorithm was originally developed for Advanced Spaceborne Thermal Emission and Reflection Radiometer (ASTER) sensor on board Terra platform. The algorithm is summarized by Gillespie et al. [9] and is described in detail in [8]. It relies on the semi-empirical relationship between the spectral contrast and the minimum spectral emissivity. The algorithm consists of three modules, namely Normalization Emissivity Module (NEM) reported by Gillespie [7], ratio module and Maximum-Minimum Difference (MMD) module reported by Matsunaga [16]. The inputs of the algorithm are land-leaving radiance L_{LL} and downwelling radiance L_{atm}^{\downarrow} . Land-leaving

radiance can be obtained from RTE by compensating for atmospheric transmissivity τ and atmospheric upwelling radiance L_{atm}^\uparrow :

$$L_{LL} = \varepsilon B(T_s) + (1 - \varepsilon)L_{atm}^\downarrow.$$

The NEM module consists of iterative process of estimating temperature and emissivity, and compensating for the downwelling radiance. The output of the NEM module is initial temperature and emissivity estimation. Then ratio module performs ratioing of the emissivities obtained by NEM module to its arithmetic mean. Thus one obtains so called β spectrum which should be less sensitive for sensor noise. Finally, maximum and minimum of β spectrum is found and its difference (MMD) is used in following relationship:

$$\varepsilon_{min} = 0.994 - 0.687 \times \text{MMD}^{0.737}. \quad (3.1)$$

Derivation of equation 3.1 is explained in following paragraph. Ratioing β spectrum back to emissivity spectrum with knowledge of minimum emissivity results in more precise emissivity estimation. The band with highest emissivity is used for temperature estimation. Such an estimation of temperature and emissivity is passed through the ratio and MMD module once again and those results are considered to be final.

The relationship between emissivity contrast and minimum spectral emissivity is regression based on 86 laboratory spectra of rocks, soils, vegetation, snow and water chosen from ASTER spectral library [1]. This relationship is shown in figure 3.1. It is important to emphasize that equation 3.1 is tailored for ASTER sensor. Nevertheless the algorithm can be applied for airborne sensors as well performing small modification. To apply temperature and emissivity separation algorithm to different sensor, regression of ε_{min} on MMD needs to be refined using sensor specific response functions. Temperature and emissivity separation algorithm was applied for example to AHS sensor as reported in [26] or to TASI sensor as reported in [19] or [28].

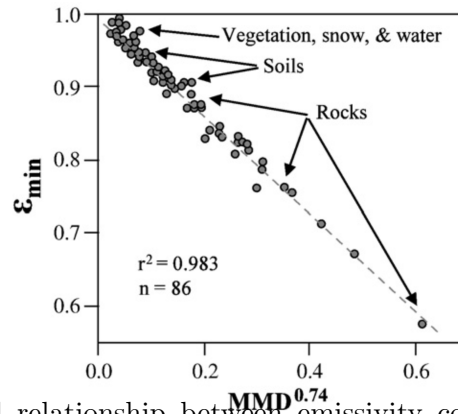


Figure 3.1: Semi-empirical relationship between emissivity contrast and minimum spectral emissivity as shown in study reported by Sabol et al. [24].

Samples with small spectral emissivity contrast are treated as gray body with constant emissivity $\varepsilon = 0.985$. These samples are detected mainly by comparing its spectral contrast with predefined MMD threshold. The MMD threshold for low-contrast samples, equation 3.1 and number of iteration in NEM module slightly differ with different versions of temperature and emissivity separation algorithm as reported by Sabol et al. [24].

3.2. TES Algorithm Improvement

The algorithm described below brings a new approach for the TES algorithm by replacing the NEM module with a completely new module. The main idea of the new module is based on the relationship between brightness temperature T_b and emissivity, where brightness temperature is the temperature obtained from land-leaving radiance under assumption of emissivity $\varepsilon = 1$. The algorithm description below omits all wavelength notation for clarity reasons. In order to demonstrate the relationship, three emissivity samples with different spectral contrasts were chosen from the ASTER spectral library [59]. These emissivities were applied to Planck's law at temperature 300 K. The resulting radiance, as well as the emissivity samples, were transformed to band-effective quantities with respect to the ASTER, AHS and TASI response functions. Brightness temperatures for every band of each sensor were obtained by applying inverse Planck's law on sample radiance under the assumption of unit emissivity. The results, shown in Fig. 3.2, clearly exhibit the relationship between emissivity and brightness temperature with linear trend, no matter what spectral contrast is or what type of sensor is used.

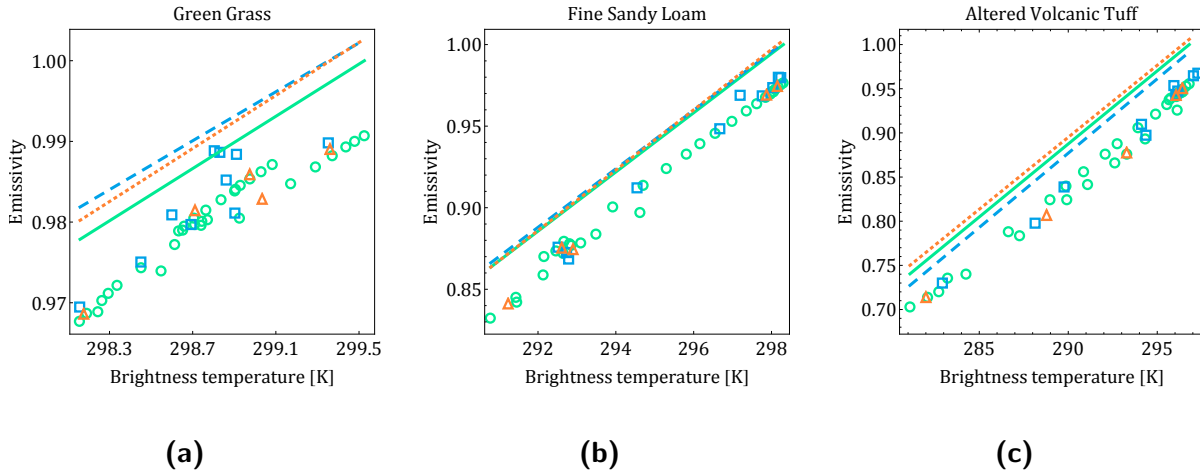


Figure 3.2: Symbols represents examples of the relationship between brightness temperature T_b and emissivity as would be observed by ASTER (orange triangles), AHS (blue squares), and TASI (green circles). Lines illustrate the approximations of the relationship between brightness temperature and emissivity for ASTER (orange dotted line), AHS (blue dashed line), and TASI (green full line) sensor. The procedure used for estimation the brightness temperature and emissivity relationship is described in text.

This property will be further used for emissivity estimation. The dependence of emissivity on brightness temperature will be approximated by following equation:

$$\varepsilon = aT_b + b, \quad (3.2)$$

where a and b are empirical coefficients. These coefficients are determined by solving the system of two equations using two points, namely maximum brightness temperature coupled with emissivity equal to 1 and minimum brightness temperature coupled with lowest emissivity ε_{\min} :

$$\begin{aligned} 1 &= a \max(T_b) + b, \\ \varepsilon_{\min} &= a \min(T_b) + b. \end{aligned} \quad (3.3)$$

The next step is estimation of the the lowest emissivity ε_{\min} .

This is done by varying ε_{\min} over the range $[0.4, 1)$, determining corresponding coefficients a and b by solving (3.3) and then approximating emissivity by (3.2) using brightness temperature for all spectral bands. The estimated emissivity is then used together with land-leaving radiance L_{LL} and downwelling radiance L^\downarrow in a computation that yields spectral radiance:

$$L' = \frac{L_{LL} - (1 - \varepsilon)L^\downarrow}{\varepsilon}. \quad (3.4)$$

The temperature in every spectral band is derived from spectral radiance L' applying inverse Planck's law. The highest one is chosen as the reference temperature T_{\max} . Finally, the estimated spectral radiance L' and Planck's law at the reference temperature T_{\max} are normalized and compared against each other as follows:

$$\sum_{\lambda_i} \left| \frac{B(T_{\max})}{\|B(T_{\max})\|_1} - \frac{L'}{\|L'\|_1} \right|, \quad (3.5)$$

where λ_i is the i -th band effective wavelength. The value of ε_{\min} is considered final if its corresponding spectral radiance L' fits Planck's law the best.

The whole process of determining ε_{\min} can be understood as smoothing the spectrum by finding the optimal value of ε_{\min} . Pseudocode depicted in Fig. ?? summarizes the above described procedure as a function $\text{SMOOTHINGERR}(\varepsilon_{\min}, L_{LL}, L^\downarrow)$ evaluating the error between Planck's law and estimated spectral radiance. This function is minimized with respect to the variable ε_{\min} as follows:

$$\arg \min_{\varepsilon_{\min} \in [0.4, 1)} \text{SMOOTHINGERR}(\varepsilon_{\min}, L_{LL}, L^\downarrow). \quad (3.6)$$

Continuous curves in Fig. 3.2 show the optimal brightness temperature and emissivity relationship approximation. Let us emphasize that the emissivity approximated by (3.2), as a result of the above described procedure, tends to be overestimated, which can be observed in the Fig. 3.2 as well. This behavior causes the temperatures, derived from spectral radiance L' , to be underestimated. Therefore the maximum temperature is likely to be the closest to the true temperature and is taken as the reference temperature.

Before passing emissivity to the Ratio and MMD modules, it is refined according to (3.7):

$$\varepsilon = \frac{L_{LL} - L^\downarrow}{B(T) - L^\downarrow}, \quad (3.7)$$

where T is the maximum temperature associated with optimal ε_{\min} . The emissivity is then further processed with the Ratio and MMD modules, with minor changes to original version of the TES algorithm as it is described in [47] and [63]. These changes include: 1) there is no refinement of ε_{\max} according to the emissivity spectral contrast, 2) the threshold T_1 for separation emissivities with small spectral contrast is not applied, and 3) the number of MMD iterations is set to one. Let us emphasize, that before reporting algorithm outputs, emissivity is refined by (3.7) using final value of temperature.

3.3. Algorithm Performance

The OSTES algorithm was tested on synthetic data and on data acquired with the ASTER sensor. The results show that the OSTES algorithm improves temperature and emissivity

Table 3.1: Standard deviations of temperature errors obtained by applying OSTES and TES algorithm on simulated data as seen by ASTER, AHS and TASI grouped according to the sample Maximum-Minimum emissivity Difference (MMD).

Sensor	MMD	OSTES	TES
ASTER	< 0.021	0.25	0.50
	> 0.021	0.36	0.43
AHS	< 0.052	0.13	0.20
	> 0.052	0.20	0.19
TASI	< 0.026	0.16	0.32
	> 0.026	0.32	0.30

retrievals in several ways. The most significant improvement occurs for surfaces with low spectral contrast, which is one of the major weaknesses of the original version of TES algorithm. The temperature and emissivity estimations from OSTES are more accurate in these cases. The investigation of OSTES with simulated data also shows that the algorithm is less sensitive to seasonal fluctuations in atmospheric and surface temperature.

3.4. Simulated Data

A data set of 6588 samples was artificially created to compare the performance of the TES and OSTES algorithms. Samples include 108 different natural surfaces chosen from ASTER spectral library [59] at different temperatures coupled with 61 different atmospheric conditions taken from TIGR (TOVS Initial Guess Retrieval) database [64, 65]. These samples were processed to land-leaving and downwelling radiance, as standard TES algorithm input, and they were transformed to band-effective quantities with respect to the ASTER, AHS and TASI response functions.

Simulated data for the ASTER sensor were processed with current implementation¹ of TES, as it is used for generation of ASTER standard products AST_05 and AST_08 [62]. The version of the original TES algorithm in cases of AHS and TASI sensors was implemented in a manner similar to that described in [49]. In addition, the implementation omits the ε_{\max} refinement for emissivities with low spectral contrast. The OSTES was applied to all sensors as it is described in previous section.

Samples were passed to the TES and OSTES algorithms and the temperature and emissivity results were compared with true values. We divide the results into two groups according to the emissivity spectral contrast. For each sensor type we determined a threshold for Maximum-Minimum emissivity Difference (MMD) in order to separate the samples with small spectral contrast such as water, vegetation, snow or samples with small particle sizes from other samples with higher spectral contrast. The threshold was determined for each sensor separately since different response functions and spectral ranges result in different MMD values for the same sample. The performance of both TES versions was determined by subtracting retrieved temperature from true temperature

¹We were unable to obtain the original TES code, so we have implemented it according to the ATBD [63] with revisions as described in [60] and [61]. We were, however, successful in getting our simulated data processed with the operational TES code.

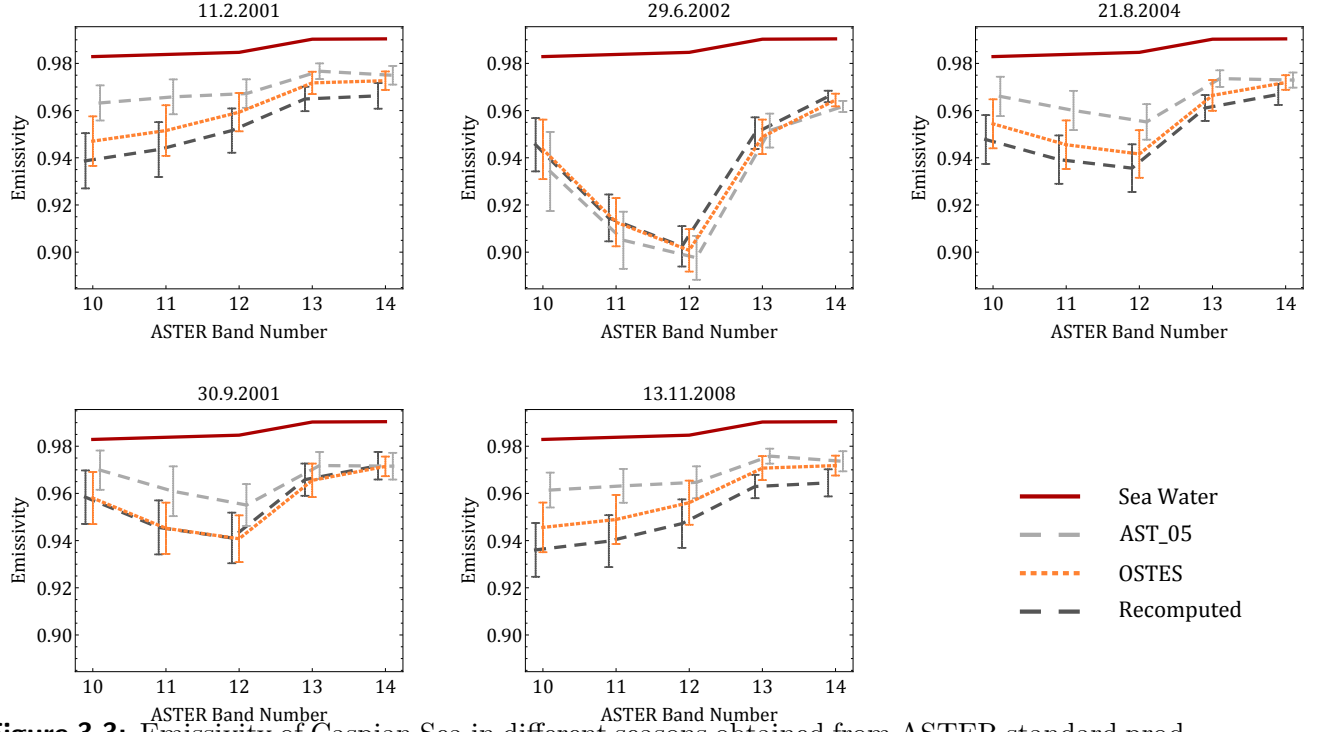


Figure 3.3: Emissivity of Caspian Sea in different seasons obtained from ASTER standard product AST_05, OSTES retrieval, and emissivity recomputation according to the temperature from AST_08 and land-leaving and downwelling radiance from AST_09T. Emissivities were extracted from area of size 40×40 pixels over pure and cloudless waterbody. Error bars display standard deviation.

value. The temperature error and chosen MMD values for ASTER, AHS and TASI are shown in Fig. ??.

It can be seen that temperature and emissivity retrieved with OSTES are more accurate for samples with low spectral contrast. On the other hand, no significant improvement is evident in cases of samples with higher spectral contrast.

Let us remind the reader that every sample is processed under several different atmospheric conditions coupled with different sample temperatures. Thus the standard deviation of temperature and emissivity error is indicative of the algorithm's sensitivity to seasonal fluctuations. A comparison of standard deviations of temperature errors introduced by both TES approaches reveals that the OSTES is less sensitive to changes in atmosphere and sample temperature for samples with low MMD. However, the standard deviations of temperature errors of samples with higher MMD are similar. Standard deviations of temperature errors obtained by the OSTES and TES algorithms are summarized in the Table 3.1.

3.5. Comparison with ASTER standard products

The performance of the OSTES algorithm was also tested and compared with standard ASTER products. Testing is focused on: 1) investigating the impact of seasonal changes on emissivity retrievals, and 2) emissivity smoothness over homogeneous areas. Both tasks were performed on ASTER scenes containing large water bodies. For the first task we chose five scenes of the Caspian Sea acquired in various seasons of the year. For

Table 3.2: ASTER scenes used for algorithm testing

Location	Acq date	Processing date
Caspian Sea	11.02.2001 - 07:35:55 (UTC)	19.11.2015
Caspian Sea	30.09.2001 - 07:35:57 (UTC)	19.11.2015
Caspian Sea	29.06.2002 - 07:31:47 (UTC)	19.11.2015
Caspian Sea	21.08.2004 - 07:29:35 (UTC)	19.11.2015
Caspian Sea	13.11.2008 - 07:24:21 (UTC)	19.11.2015
Lake Baikal	22.07.2002 - 04:17:29 (UTC)	27.08.2015

the second task we chose Lake Baikal. The list of all scenes used, together with their acquisition and processing date is given in Table 3.2. For every scene we downloaded ASTER standard products AST_09T, AST_08 and AST_05 delivering land-leaving and downwelling radianace, surface kinetic temperature and surface emissivity, respectively. Product AST_09T was used as input to the OSTES algorithm. The resulting temperature and emissivity was then compared with the AST_08 and AST_05 standard products. The emissivity variability over large and homogeneous area was chosen to be the quality indicator, since we are interested in the retrieval of material properties, which should be constant within the time and space.

From the Caspian Sea scenes we chose samples of size 40×40 pixels over uniform, cloudless waterbody. These subsets were processed by the OSTES algorithm and the emissivity results were averaged for every scene. The results are plotted in Fig. 3.3 along with the emissivities that were delivered in the AST_05 product and averaged over the same spatial subset. In most cases the AST_05 emissivity spectra appear to be closer to the sea water emissivity spectra taken from ASTER spectral library [59]. However, the temperature retrievals of extracted samples obtained by OSTES and TES are very close (not shown). The average temperature difference of AST_08 and OSTES results computed from all Caspian Sea samples is 0.2 K (s.d. 0.2 K). The fact that the temperatures obtained with the two algorithms are very close, but the emissivities are not implies that the emissivity spectra from AST_05 product are not consistent with temperature from AST_08 product. We verified this inconsistency by taking the temperatures delivered in AST_08 and the downwelling and land-leaving radiances delivered in AST_09T and putting these into (3.7) to obtain emissivities that are different from what is in the AST_05 product. These emissivity spectra derived from AST_08 and AST_09T, which we refer to as “recomputed emissivities”, are depicted on Fig. 3.3 as well. Comparing recomputed emissivity spectra and OSTES results shows that in scenes acquired on 29.6.2002 and 30.9.2001 are results similar. On the other hand OSTES results perform slightly better in scenes acquired on 11.2.2001, 21.8.2004 and 13.11.2008. Nevertheless, none of the emissivity spectra agrees with expected values.

The difference in emissivity obtained by the two versions of TES is further illustrated in the scene over Lake Baikal shown in Fig. 3.4. In this figure the white squares on the images define a water body sample of size 90×90 pixels that was used to produce the values in the histograms below the images. The expected values of sea water emissivity (red vertical line) are included in the Fig. 3.4. The histograms show the OSTES emissivity retrievals compared against the AST_05 standard product, as well as the emissivity recomputed

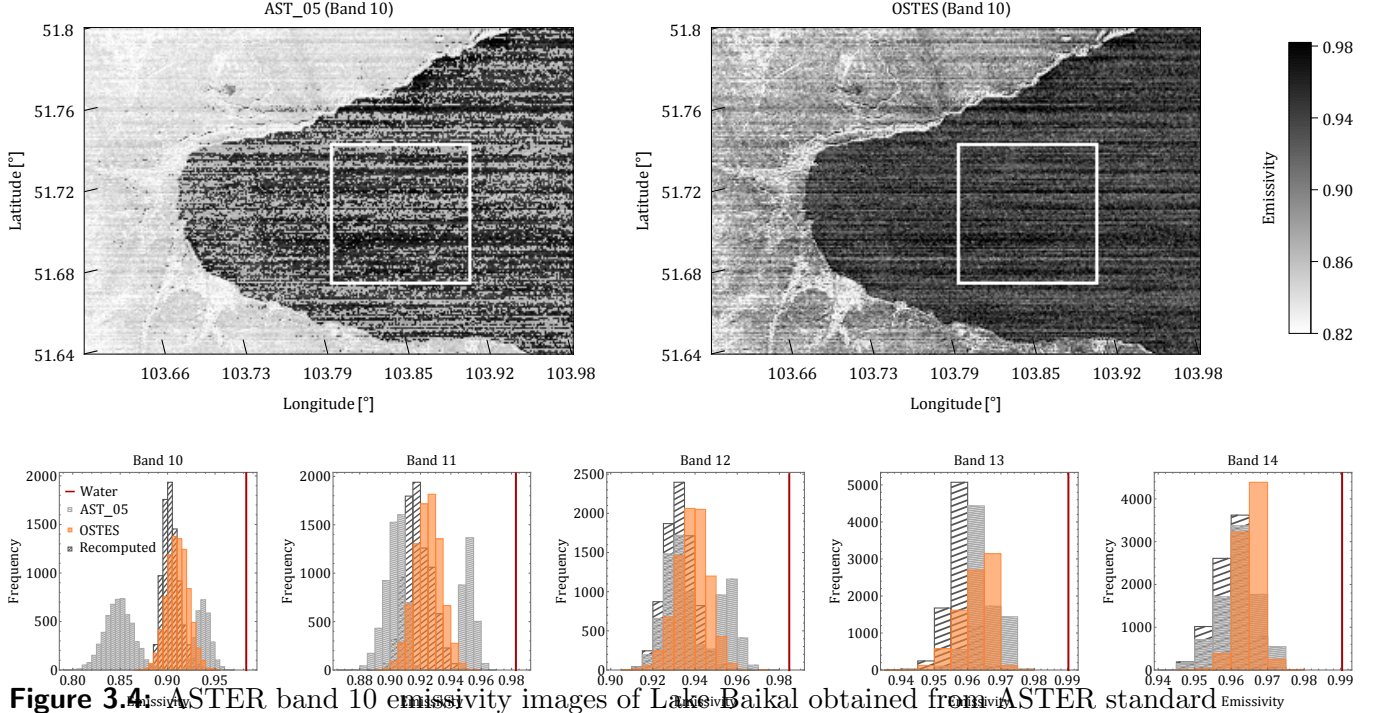


Figure 3.4: ASTER band 10 emissivity images of Lake Baikal obtained from ASTER standard product AST_05 (upper left) and OSTES emissivity retrieval (upper right). In both images the same contrast stretching is used. The white square represents the area from which emissivity histograms were created (lower panel). Histograms show distributions of AST_05 emissivity, OSTES emissivity and recomputed emissivity according to the temperature from AST_08 and land-leaving and downwelling radiance from AST_09T. Line depicted in histograms indicates the expected value of water emissivity retrieved from ASTER spectral library [59].

with respect to the temperature delivered by AST_08 and land-leaving and downwelling radiance delivered by AST_09T, as described in the previous paragraph. Inspection of the ASTER standard product AST_05 shows step discontinuities in bands 10, 11 and 12 over the study sample, which is reflected in the bimodal distributions in the histograms and the noisy patterns in the left image. On the contrary, OSTES emissivity results are smoother and the histograms do not show any significant discontinuities. The recomputed and OSTES emissivity retrievals are similar. However, the OSTES emissivities tend to be closer to the expected values. In addition to the noise, striping is also visible in the image. This not consequence of the TES algorithm and is more deeply discussed in [66]. Even though the AST_05 and OSTES emissivities differ significantly in some bands, the temperature retrievals are very similar. The average difference is 0.25 K (s.d. 0.18 K). Similar to the discussion regarding Caspian Sea emissivity retrievals, it can also be concluded in this case that none of the emissivity spectra have satisfying values.

The discrepancies in shape and magnitude of emissivity spectra can be caused by various source of errors but the main error source has been attributed to imperfect atmospheric corrections. The impact of this error is evident mainly in cases of low spectral constast. Notable works discussing emissivity retrievals with low spectral contrast are [67, 68, 69, 70, 71]. One suggested improvement is the water vapour scaling method [72, 66].

The step discontinuities in emissivity values over homogeneous area can occur due to various thresholds deciding how to treat the sample during processing. The original TES algorithm starts in the NEM module assuming a maximum emissivity spectra $\varepsilon_{\max} = 0.99$.

The NEM module is then restarted with refined ε_{\max} according to the emissivity retrieved from the first NEM pass. Also, temperature and emissivity from NEM are reported as the result of TES algorithm if the correction for downwelling radiance is not possible. The original version of TES processes samples according to the MMD of emissivity spectra obtained from NEM module either by incorporating (3.1) or by presetting emissivity to $\varepsilon = 0.983$. Some authors [60], [61] have suggested that the value of the threshold used for classifying observations into groups with either low or high spectral contrast should be changed or completely removed. Observations with wrongly determined spectral contrast or observations with spectral contrast close to any threshold result in step discontinuities. On the contrary, the OSTES does not set any thresholds for materials with low spectral contrast and so it is expected to generate smoother results on homogeneous areas with low spectral contrast.

3.6. Application to TASI Data

4

Ground Measurements

4.1. Libraries

4.2. Technical Specifications

4.3. Instrument Calibration

4.4. Temperature and Emissivity Separation

4.5. Applications

5

Application to UHI Detection

6

Conclusion

Own publications

References

- [1] BALDRIDGE, A.M., S.J. HOOK, C.I. GROVE and G. RIVERA. The ASTER spectral library version 2.0. *Remote Sensing of Environment*. 2009, vol. 113, issue 4, s. 711-715 [cit. 2015-04-24]. DOI: 10.1016/j.rse.2008.11.007.
- [2] BARDUCCI, A. and I. PIPPI. Temperature and emissivity retrieval from remotely sensed images using the "Grey body emissivity" method. *IEEE Transactions on Geoscience and Remote Sensing*. vol. 34, issue 3, s. 681-695. DOI: 10.1109/36.499748. Dostupné z: <http://ieeexplore.ieee.org/lpdocs/epic03/wrapper.htm?arnumber=499748>
- [3] BERK, A., G.P. ANDERSON, P.K. ACHARYA, L.S. BERNSTEIN, L. MURATOV, J. LEE, M. FOX, S.M. ADLER-GOLDEN, J.H. CHETWYND, JR., M.L. HOKE, R.B. LOCKWOOD, J.A. GARDNER, T.W. COOLEY, C.C. BOREL, P.E. LEWIS and E.P. SHETTL. MODTRAN5: 2006 update. In: *Algorithms and Technologies for Multispectral, Hyperspectral, and Ultraspectral Imagery XII*. 2006 [cit. 2015-04-24]. DOI: 10.1117/12.665077.
- [4] BORBAS, E., S.W. SEEMANN, KERN, MOY, J. LI, L. GUMLEY and W.P. MENZEL. MODIS Atmospheric Profile Retrieval - ATBD. 2011.
- [5] BOREL, C.C. Surface emissivity and temperature retrieval for a hyperspectral sensor. IGARSS '98. Sensing and Managing the Environment. *IEEE International Geoscience and Remote Sensing*. Symposium Proceedings. (Cat. No.98CH36174). IEEE, 1998, 546-549 vol.1. DOI: 10.1109/IGARSS.1998.702966. Available at: <http://ieeexplore.ieee.org/lpdocs/epic03/wrapper.htm?arnumber=702966>
- [6] BOREL, C. Error analysis for a temperature and emissivity retrieval algorithm for hyperspectral imaging data. *International Journal of Remote Sensing* [online]. 2008, vol. 29, 17-18, s. 5029-5045 [cit. 2015-04-24]. DOI: 10.1080/01431160802036540.
- [7] GILLESPIE, A. R., 1986. Lithologic mapping of silicate rocks using TIMS. Dostupné z: <http://ntrs.nasa.gov/search.jsp?R=19870007685>
- [8] GILLESPIE, A., S. ROKUGAWA, S. HOOK, T. MATSUNAGA and A.B. KAHLE. *Temperature/Emissivity Separation Algorithm Theoretical Basis Document, Version 2.4*. Pasadena: Jet Propulsion Laboratory, 1999, 64 p.
- [9] GILLESPIE, A., S. ROKUGAWA, T. MATSUNAGA, J.S. COTHERN, S. HOOK and A.B. KAHLE. A temperature and emissivity separation algorithm for Advanced Spaceborne Thermal Emission and Reflection Radiometer (ASTER) images. *IEEE*

- Transactions on Geoscience and Remote Sensing* [online]. 1998, vol. 36, issue 4, s. 1113-1126 [cit. 2015-04-24]. DOI: 10.1109/36.700995.
- [10] GU, D., A.R. GILLESPIE, A.B. KAHLE and F.D. PALLUCONI. Autonomous atmospheric compensation (AAC) of high resolution hyperspectral thermal infrared remote-sensing imagery. *IEEE Transactions on Geoscience and Remote Sensing*. 2000, vol. 38, issue 6, s. 2557-2570 [cit. 2015-04-24]. DOI: 10.1109/36.885203.
- [11] HANUŠ, J., T. FABIÁNEK, V. KAPLAN a L. HOMOLOVÁ. FLYING LABORATORY OF IMAGING SYSTEMS (FLIS) AT CZECHGLOBE. In: SGEM2014 Conference Proceedings. 2014, s. 177-182. DOI: 10.5593/SGEM2014/B23/S10.022. ISBN 978-619-7105-12-4. ISSN 1314-2704.
- [12] HOWELL, J.R. Thermal radiation heat transfer. 5th ed. Boca Raton: CRC Press, c2011, 957 s. ISBN 978-1-4398-0533-6.
- [13] JONG, Edited by F.D. van der MEER and STEVEN M. de. Imaging spectrometry basic principles and prospective applications: basic principles and prospective applications. [Nachdr.]. Dordrecht: Springer, 2013. ISBN 978-0-306-47578-8.
- [14] KIRCHHOFF, G. Ueber das Verhältniss zwischen dem Emissionsvermögen und dem Absorptionsvermögen der Körper für Wärme und Licht. *Annalen der Physik und Chemie*. 1860, vol. 185, issue 2, s. 275-301 [cit. 2015-04-24]. DOI: 10.1002/andp.18601850205.
- [15] LI, Z., B. TANG, H. WU, H. REN, G. YAN, Z. WAN, I.F. TRIGO and J.A. SOBRINO. Satellite-derived land surface temperature: Current status and perspectives. *Remote Sensing of Environment* [online]. 2013, vol. 131, s. 14-37 [cit. 2015-04-24]. DOI: 10.1016/j.rse.2012.12.008.
- [16] MATSUNAGA, T., 1994. A Temperature-Emissivity Separation Method Using an Empirical Relationship between the Mean, the Maximum, and the Minimum of the Thermal Infrared Emissivity Spectrum. *Journal of the Remote Sensing Society of Japan*. vol. 14, i. 3, p. 230-241. Available at: doi:10.11440/rssj1981.14.230
- [17] MODIS website [online]. [cit. 2015-05-06]. Dostupné z: <http://modis.gsfc.nasa.gov/>
- [18] NOTESCO, G., V. KOPAČKOVÁ, P. ROJÍK, G. SCHWARTZ, I. LIVNE and E. DOR. Mineral Classification of Land Surface Using Multispectral LWIR and Hyperspectral SWIR Remote-Sensing Data. A Case Study over the Sokolov Lignite Open-Pit Mines, the Czech Republic. *Remote Sensing*. 2014, vol. 6, issue 8, s. 7005-7025. DOI: 10.3390/rs6087005. Available at: <http://www.mdpi.com/2072-4292/6/8/7005/>
- [19] PIPIA, L., F. PEREZ, A. TARDA, L. MARTINEZ and R. ARBIOL. Simultaneous usage of optic and thermal hyperspectral sensors for crop water stress characterization. 2012 *IEEE International Geoscience and Remote Sensing Symposium*. IEEE, 2012, s. 6661-6664. DOI: 10.1109/IGARSS.2012.6352071. Available at: <http://ieeexplore.ieee.org/lpdocs/epic03/wrapper.htm?arnumber=6352071>
- [20] PLANCK, M. Zur Theorie des Gesetzes der Energieverteilung im Normalspektrum. *Verhandlungen der Deutschen Physikalischen Gesellschaft*. 1900, vol. 2, p. 237

- [21] POGORZALA, D., D. MESSINGER, C. SALVAGGIO and J. SCHOTT, 2005. Gas plume species identification in airborne LWIR imagery using constrained stepwise regression analyses. s. 194–205, Available at: doi:10.1117/12.603661
- [22] RIBEIRO DA LUZ, B. and J.K. CROWLEY. Identification of plant species by using high spatial and spectral resolution thermal infrared (8.0–13.5 μm) imagery. *Remote Sensing of Environment*. 2010, vol. 114, issue 2, s. 404–413. DOI: 10.1016/j.rse.2009.09.019. Available at: <http://linkinghub.elsevier.com/retrieve/pii/S0034425709002910>
- [23] RICHTER, R. a D. SCHLÄPFER. Geo-atmospheric processing of airborne imaging spectrometry data. Part 2: Atmospheric/topographic correction. *International Journal of Remote Sensing*. 2002, 23(13), 2631–2649. DOI: 10.1080/01431160110115834. ISSN 0143-1161.
- [24] SABOL, Jr., D.E., A. R. GILLESPIE, E. ABBOTT and G. YAMADA. Field validation of the ASTER Temperature–Emissivity Separation algorithm. *Remote Sensing of Environment*. 2009-11-16, vol. 113, issue 11, s. 2328–2344. DOI: 10.1016/j.rse.2009.06.008. Available at: <http://linkinghub.elsevier.com/retrieve/pii/S0034425709001898>
- [25] SOBRINO, J. A., B. FRANCH, C. MATTAR, J. C. JIMÉNEZ-MUÑOZ and C. CORBARI, 2012. A method to estimate soil moisture from Airborne Hyperspectral Scanner (AHS) and ASTER data: Application to SEN2FLEX and SEN3EXP campaigns. *Remote Sensing of Environment*. 15.2., roč. 117, s. 415–428. ISSN 0034-4257. Available at: doi:10.1016/j.rse.2011.10.018
- [26] SOBRINO, J. A., J. C. JIMÉNEZ-MUÑOZ, P. J. ZARCO-TEJADA, G. SEPULCRE-CANTÓ and DE MIGUEL. Land surface temperature derived from airborne hyperspectral scanner thermal infrared data. *Remote Sensing of Environment*. 2006, vol. 102, 1-2. DOI: 10.1016/j.rse.2006.02.001.
- [27] SOBRINO, J. A., R. OLTRA-CARRIÓ, J. C. JIMÉNEZ-MUÑOZ, Y. JULIEN, G. SÒRIA, B. FRANCH and C. MATTAR, 2012. Emissivity mapping over urban areas using a classification-based approach: Application to the Dual-use European Security IR Experiment (DESIREX). *International Journal of Applied Earth Observation and Geoinformation*. vol. 18, i. 0, s. 141–147. Available at: doi:<http://dx.doi.org/10.1016/j.jag.2012.01.022>
- [28] WANG, H., Q. XIAO, H. LI and B. ZHONG. Temperature and emissivity separation algorithm for TASI airborne thermal hyperspectral data. In: *2011 International Conference on Electronics, Communications and Control (ICECC)*. 2011 [cit. 2015-04-24]. DOI: 10.1109/icecc.2011.6066288.
- [29] WANG, N., H. WU, F. NERRY, C. LI and Z. LI. Temperature and Emissivity Retrievals From Hyperspectral Thermal Infrared Data Using Linear Spectral Emissivity Constraint. *IEEE Transactions on Geoscience and Remote Sensing*. 2011, vol. 49, issue 4, s. 1291–1303. DOI: 10.1109/TGRS.2010.2062527. Available at: <http://ieeexplore.ieee.org/lpdocs/epic03/wrapper.htm?arnumber=5567152>

- [30] YOUNG, S.J. An in-scene method for atmospheric compensation of thermal hyperspectral data. *Journal of Geophysical Research*. 2002, vol. 107, D24 [cit. 2015-04-24]. DOI: 10.1029/2001jd001266.
- [31] ZEMEK, František. *Airborne remote sensing: theory and practice in assessment of terrestrial ecosystems*. Brno: Global Change Research Centre AS CR, c2014, 159 s. ISBN 978-80-87902-05-9.
- [32] F. D. van der Meer, H. M. A. van der Werff, F. J. A. van Ruitenbeek, C. A. Hecker, W. H. Bakker, M. F. Noomen, M. van der Meijde, E. J. M. Carranza, J. B. d. Smeth, and T. Woldai, “Multi- and hyperspectral geologic remote sensing: A review,” *International Journal of Applied Earth Observation and Geoinformation*, vol. 14, no. 1, pp. 112–128, Feb. 2012.
- [33] D. Pieri and M. Abrams, “ASTER watches the world’s volcanoes: a new paradigm for volcanological observations from orbit,” *Journal of Volcanology and Geothermal Research*, vol. 135, no. 1–2, pp. 13–28, Jul. 2004.
- [34] L. Foster, B. Brock, M. Cutler, and F. Diotri, “A physically based method for estimating supraglacial debris thickness from thermal band remote-sensing data,” *Journal of Glaciology*, vol. 58, no. 210, pp. 677–691, Aug. 2012.
- [35] S. Scheidt, M. Ramsey, and N. Lancaster, “Determining soil moisture and sediment availability at white sands dune field, new mexico, from apparent thermal inertia data,” *Journal of Geophysical Research: Earth Surface*, vol. 115, no. F2, pp. n/a–n/a, 2010, f02019.
- [36] Q. Weng, U. Rajasekar, and X. Hu, “Modeling Urban Heat Islands and Their Relationship With Impervious Surface and Vegetation Abundance by Using ASTER Images,” *IEEE Transactions on Geoscience and Remote Sensing*, vol. 49, no. 10, pp. 4080–4089, Oct. 2011.
- [37] A. N. French, T. J. Schmugge, J. C. Ritchie, A. Hsu, F. Jacob, and K. Ogawa, “Detecting land cover change at the Jornada Experimental Range, New Mexico with ASTER emissivities,” *Remote Sensing of Environment*, vol. 112, no. 4, pp. 1730–1748, Apr. 2008.
- [38] G. Notesco, V. Kopačková, P. Rojík, G. Schwartz, I. Livne, and E. B. Dor, “Mineral Classification of Land Surface Using Multispectral LWIR and Hyperspectral SWIR Remote-Sensing Data. A Case Study over the Sokolov Lignite Open-Pit Mines, the Czech Republic,” *Remote Sensing*, vol. 6, no. 8, pp. 7005–7025, Jul. 2014.
- [39] J. A. Sobrino, B. Franch, C. Mattar, J. C. Jiménez-Muñoz, and C. Corbari, “A method to estimate soil moisture from Airborne Hyperspectral Scanner (AHS) and ASTER data: Application to SEN2flex and SEN3exp campaigns,” *Remote Sensing of Environment*, vol. 117, pp. 415–428, Feb. 2012.
- [40] J. A. Sobrino, R. Oltra-Carrió, J. C. Jiménez-Muñoz, Y. Julien, G. Sòria, B. Franch, and C. Mattar, “Emissivity mapping over urban areas using a classification-based approach: Application to the Dual-use European Security IR Experiment (DESIREX),”

- International Journal of Applied Earth Observation and Geoinformation*, vol. 18, pp. 141–147, Aug. 2012.
- [41] S. Pascucci, R. Casa, C. Belviso, A. Palombo, S. Pignatti, and F. Castaldi, “Estimation of soil organic carbon from airborne hyperspectral thermal infrared data: A case study,” *European Journal of Soil Science*, vol. 65, no. 6, pp. 865–875, 2014.
 - [42] L. Pipia, F. Perez, A. Tarda, L. Martinez, and R. Arbiol, “Simultaneous usage of optic and thermal hyperspectral sensors for crop water stress characterization,” in *Geoscience and Remote Sensing Symposium (IGARSS), 2012 IEEE International*, Jul. 2012, pp. 6661–6664.
 - [43] Z.-L. Li, B.-H. Tang, H. Wu, H. Ren, G. Yan, Z. Wan, I. F. Trigo, and J. A. Sobrino, “Satellite-derived land surface temperature: Current status and perspectives,” *Remote Sensing of Environment*, vol. 131, pp. 14–37, Apr. 2013.
 - [44] A. Barducci and I. Pippi, “Temperature and emissivity retrieval from remotely sensed images using the “Grey body emissivity” method,” *IEEE Transactions on Geoscience and Remote Sensing*, vol. 34, no. 3, pp. 681–695, May 1996.
 - [45] N. Wang, H. Wu, F. Nerry, C. Li, and Z.-L. Li, “Temperature and Emissivity Retrievals From Hyperspectral Thermal Infrared Data Using Linear Spectral Emissivity Constraint,” *IEEE Transactions on Geoscience and Remote Sensing*, vol. 49, no. 4, pp. 1291–1303, Apr. 2011.
 - [46] C. Borel, “Error analysis for a temperature and emissivity retrieval algorithm for hyperspectral imaging data,” *International Journal of Remote Sensing*, vol. 29, no. 17-18, pp. 5029–5045, Sep. 2008.
 - [47] A. Gillespie, S. Rokugawa, T. Matsunaga, J. Cothorn, S. Hook, and A. Kahle, “A temperature and emissivity separation algorithm for Advanced Spaceborne Thermal Emission and Reflection Radiometer (ASTER) images,” *IEEE Transactions on Geoscience and Remote Sensing*, vol. 36, no. 4, pp. 1113–1126, Jul. 1998.
 - [48] J. A. Sobrino, J. C. Jiménez-Muñoz, P. J. Zarco-Tejada, G. Sepulcre-Cantó, and E. de Miguel, “Land surface temperature derived from airborne hyperspectral scanner thermal infrared data,” *Remote Sensing of Environment*, vol. 102, no. 1–2, pp. 99–115, May 2006.
 - [49] J. Jiménez-Muñoz, J. Sobrino, and A. Gillespie, “Surface Emissivity Retrieval From Airborne Hyperspectral Scanner Data: Insights on Atmospheric Correction and Noise Removal,” *IEEE Geoscience and Remote Sensing Letters*, vol. 9, no. 2, pp. 180–184, Mar. 2012.
 - [50] H. Wang, Q. Xiao, H. Li, and B. Zhong, “Temperature and emissivity separation algorithm for TASI airborne thermal hyperspectral data,” in *2011 International Conference on Electronics, Communications and Control (ICECC)*, Sep. 2011, pp. 1075–1078.

BIBLIOGRAPHY

- [51] J. A. Sobrino, J. C. Jiménez-Muñoz, J. Labed-Nachbrand, and F. Nerry, "Surface emissivity retrieval from Digital Airborne Imaging Spectrometer data," *Journal of Geophysical Research-Atmospheres*, vol. 107, no. D23, p. 4729, Dec. 2002.
- [52] J. Jiménez-Muñoz, J. Sobrino, C. Mattar, G. Hulley, and F.-M. Gottsche, "Temperature and Emissivity Separation From MSG/SEVIRI Data," *IEEE Transactions on Geoscience and Remote Sensing*, vol. 52, no. 9, pp. 5937–5951, Sep. 2014.
- [53] G. Hulley and S. Hook, "Generating Consistent Land Surface Temperature and Emissivity Products Between ASTER and MODIS Data for Earth Science Research," *IEEE Transactions on Geoscience and Remote Sensing*, vol. 49, no. 4, pp. 1304–1315, Apr. 2011.
- [54] A. Mushkin, L. K. Balick, and A. R. Gillespie, "Temperature/emissivity separation of MTI data using the Terra/ASTER TES algorithm," in *Algorithms and Technologies for Multispectral, Hyperspectral, and Ultraspectral Imagery VIII*, vol. 4725, 2002, pp. 328–337.
- [55] G. Hulley and S. Hook, "HyspIRI Level-2 Thermal Infrared (TIR) Land Surface Temperature and Emissivity Algorithm Theoretical Basis Document," Jet Propulsion Laboratory, California Institute of Technology, Pasadena, California, Tech. Rep., May 2011. [Online]. Available: https://hyspiri.jpl.nasa.gov/downloads/Algorithm_Theoretical_Basis/HyspIRI_L2_Surface_Temperature_Emissivity_JPL_Pub_11-5_10102011.pdf
- [56] A. Fernández-Renau, J. A. Gómez, and E. de Miguel, "The INTA AHS system," in *SPIE Proceedings*, vol. 5978, 2005, pp. 59 781L–59 781L–8.
- [57] A. R. Gillespie, "Lithologic mapping of silicate rocks using TIMS," Jet Propulsion Lab., California Inst. of Tech., Pasadena, CA, United States, Tech. Rep., Nov. 1986.
- [58] T. Matsunaga, "A Temperature-Emissivity Separation Method Using an Empirical Relationship between the Mean, the Maximum, and the Minimum of the Thermal Infrared Emissivity Spectrum," *Journal of the Remote Sensing Society of Japan*, vol. 14, no. 3, pp. 230–241, 1994.
- [59] A. M. Baldridge, S. J. Hook, C. I. Grove, and G. Rivera, "The ASTER spectral library version 2.0," *Remote Sensing of Environment*, vol. 113, no. 4, pp. 711–715, Apr. 2009.
- [60] W. T. Gustafson, A. R. Gillespie, and G. J. Yamada, "Revisions to the ASTER temperature/emissivity separation algorithm," *Second Recent Advances in Quantitative Remote Sensing*, pp. 770–775, 2006.
- [61] J. Sabol, Donald E., A. R. Gillespie, E. Abbott, and G. Yamada, "Field validation of the ASTER Temperature–Emissivity Separation algorithm," *Remote Sensing of Environment*, vol. 113, no. 11, pp. 2328–2344, Nov. 2009.
- [62] B. Eng, personal communication, 2015.

- [63] A. R. Gillespie, S. Rokugawa, S. J. Hook, T. Matsunaga, and A. B. Kahle, “Temperature/Emissivity Separation Algorithm Theoretical Basis Document, Version 2.4,” Tech. Rep., Mar. 1999. [Online]. Available: <http://www.science.aster.ersdac.jspacesystems.or.jp/en/documnts/pdf/2b0304.pdf>
- [64] A. Chedin, N. A. Scott, C. Wahiche, and P. Moulinier, “The Improved Initialization Inversion Method: A High Resolution Physical Method for Temperature Retrievals from Satellites of the TIROS-N Series,” *Journal of Climate and Applied Meteorology*, vol. 24, no. 2, pp. 128–143, Feb. 1985.
- [65] F. Chevallier, F. Chérut, N. A. Scott, and A. Chédin, “A Neural Network Approach for a Fast and Accurate Computation of a Longwave Radiative Budget,” *Journal of Applied Meteorology*, vol. 37, no. 11, pp. 1385–1397, Nov. 1998.
- [66] A. R. Gillespie, E. A. Abbott, L. Gilson, G. Hulley, J.-C. Jiménez-Muñoz, and J. A. Sobrino, “Residual errors in ASTER temperature and emissivity standard products AST08 and AST05,” *Remote Sensing of Environment*, vol. 115, no. 12, pp. 3681–3694, Dec. 2011.
- [67] H. Tonooka and F. D. Palluconi, “Verification of the ASTER/TIR atmospheric correction algorithm based on water surface emissivity retrieved,” in *Infrared Spaceborne Remote Sensing IX*, M. Strojnik and B. F. Andresen, Eds. Bellingham: Spie-Int Soc Optical Engineering, 2001, vol. 4486, pp. 51–58.
- [68] H. Tonooka and F. Palluconi, “Validation of ASTER/TIR standard atmospheric correction using water surfaces,” *IEEE Transactions on Geoscience and Remote Sensing*, vol. 43, no. 12, pp. 2769–2777, Dec. 2005.
- [69] H. Tonooka, F. Palluconi, S. Hook, and T. Matsunaga, “Vicarious calibration of ASTER thermal infrared bands,” *IEEE Transactions on Geoscience and Remote Sensing*, vol. 43, no. 12, pp. 2733–2746, Dec. 2005.
- [70] C. Coll, V. Caselles, E. Valor, R. Niclòs, J. M. Sánchez, J. M. Galve, and M. Mira, “Temperature and emissivity separation from ASTER data for low spectral contrast surfaces,” *Remote Sensing of Environment*, vol. 110, pp. 162–175, Sep. 2007.
- [71] J. A. Sobrino, J. C. Jiménez-Muñoz, L. Balick, A. R. Gillespie, D. A. Sabol, and W. T. Gustafson, “Accuracy of ASTER level-2 thermal-infrared standard products of an agricultural area in Spain,” *Remote Sensing of Environment*, vol. 106, no. 2, pp. 146–153, Jan. 2007.
- [72] H. Tonooka, “Accurate atmospheric correction of ASTER thermal infrared imagery using the WVS method,” *IEEE Transactions on Geoscience and Remote Sensing*, vol. 43, no. 12, pp. 2778–2792, Dec. 2005.
- [73] ITRES. SparCal [software]. [access 1.3.2016]. Available at: <http://www.itres.com/supporting-products/>
- [74] ITRES. RCX [software]. [access 1.3.2016]. Available at: <http://www.itres.com/supporting-products/>

BIBLIOGRAPHY

- [75] ITRES. GCSS [software]. [access 1.3.2016]. Available at:
<http://www.itres.com/supporting-products/>